A region growing method for detecting interfaces in X-ray view cell images

Phanindra Jampana, Sirish Shah and John Shaw

***Abstract*—X-ray transmission videography is used to observe the thermodynamic phase behavior of heavy oil mixtures of industrial interest that are opaque to visible light. The knowledge of the volumes of various phases provide important information for enhancing oil refining technology. Phase boundaries are usually marked by visual examination based upon which the volumes and densities of the phases are computed. Typically phase behavior is computed at various temperatures and pressures to generate the phase diagram. This paper presents an image processing algorithm which automates the task of detecting phase boundaries in the generated images. The interface and region models are first obtained from the image generation process. Using these models a new method for interface detection based on the Mumford-Shah model is presented. Results are presented to show that the algorithm detects the phase boundaries to sub-pixel accuracy.**

***Index Terms*—X-ray view-cell, image processing, automatic boundary detection**

I. Introduction

Information about the phase behavior of heavy oil mixtures such as Bitumen + Water and Athabasca Vacuum Bottoms (ABVB) + pentane, decane and hydrogen at various temperatures and pressures can be used to optimize existing technologies and develop novel methods for Bitumen production and refining. Due to this reason, there is significant interest in obtaining the phase behavior data in the form of phase diagrams. Standard instruments for measuring phase behavior are based on view cells employing visible or infrared light. It has been observed that these techniques fail to identify all bulk phases present due to the opacity of the mixtures e.g. when asphaltene mass fractions exceed 5 wt%. A recent method to overcome the limitations of the traditional instruments is by the use of X-rays in place of infrared or visible light (Abedi et al. (1999)). Prior to this technology the phase behavior of important mixtures could not be computed.

The X-ray view cell apparatus is already being successfully employed to obtain phase behavior data. For example, the effect of phase behavior of ABVB + Decane + Hydrogen on coke deposition of catalyst used for hydro-treating is studied in (Zhang & Shaw (2006)). The phase behavior of Bitumen + Water mixtures has recently been reported by (Mohammad et al. (2013)). In both the cases, the images resulting from the X-ray view cell have been analyzed manually to obtain the phase data.

The X-ray view cell consists of a 0.15m long, 0.17m outside diameter/0.05 inside diameter Beryllium tube that is bolted to stainless steel plates at the top and bottom (Beryllium is virtually transparent to X-rays due to its low density and absorbency). The top plate is attached to a stainless steel bellows for varying the internal volume. A Beryllium *insert* which permits detection of small volumes of dense liquid phases is attached to the bottom plate. Above this insert sits a magnetic stirrer, which is used to mix and homogenize the sample. The cell is surrounded by a programmable, refractory-lined heating-jacket. The sample is contained inside the hollow portion of the Beryllium tube and transmitted X-ray images of the whole setup are obtained (Zou & Shaw (2006); Abedi et al. (1999)). The complete schematic is shown in Figure 1 (Abedi (1998)) (In this Figure, ADC refers to the Analog to Digital Converter).

Fig 2 shows the individual components of the view cell as described above. The slotted plate in Fig 2b is used to restrict the stirrer from falling into the insert. The top plate is clasped to the upper part of the view cell and the insert along with the slotted plate and the stirrer is fitted into the hollow part of the view cell at the bottom. The stirrer is then operated using an external magnetic field. X-ray images of the whole setup are obtained.

The intensity of X-ray decreases due to photoelectric absorption in the medium. Absorption increases with the thickness, density and the mass absorption coefficient of the medium. This process is mathematically explained by Beer's Law :- For monochromatic X-ray's of wavelength λ,

$$I(\lambda) = I_0(\lambda) \exp\{-\rho \Delta x \mu(\lambda)\} \tag{1}$$

where $I(\lambda), I_0(\lambda)$ are the intensities of the transmitted and incident X-ray beam and $\Delta x, \rho, \mu(\lambda)$ are the path length, density of the medium and the mass absorption coefficient respectively. For poly-chromatic X-rays,

$$\sum_i I(\lambda_i) = \sum_i I_0(\lambda_i) \exp\{-\rho \Delta x \sum_k w_k \mu_{k,i}\} \tag{2}$$

where λ_i's are the different wavelengths and $\sum_k w_k \mu_{k,i}$ is the weighted average of mass absorption coefficients of the constituent elements of the substance at wavelength λ_i.

The change in the intensity due to the image intensifier and the imaging lens (the detector) (Fig 1) is independent of the sample present in the view cell. Hence, all the observed image intensities are scaled by the same amount. This scaling

Phanindra Jampana is with the Department of Chemical Engineering, Indian Institute of Technology Hyderabad, Yeddumailaram, Medak, A.P., India, 502205, e-mail: pjampana@iith.ac.in

Sirish Shah and John Shaw are with the Department of Chemical Engineering, University of Alberta, Edmonton, Canada T6G1H7, e-mail:sirish.shah@ualberta.ca, jmshaw@ualberta.ca

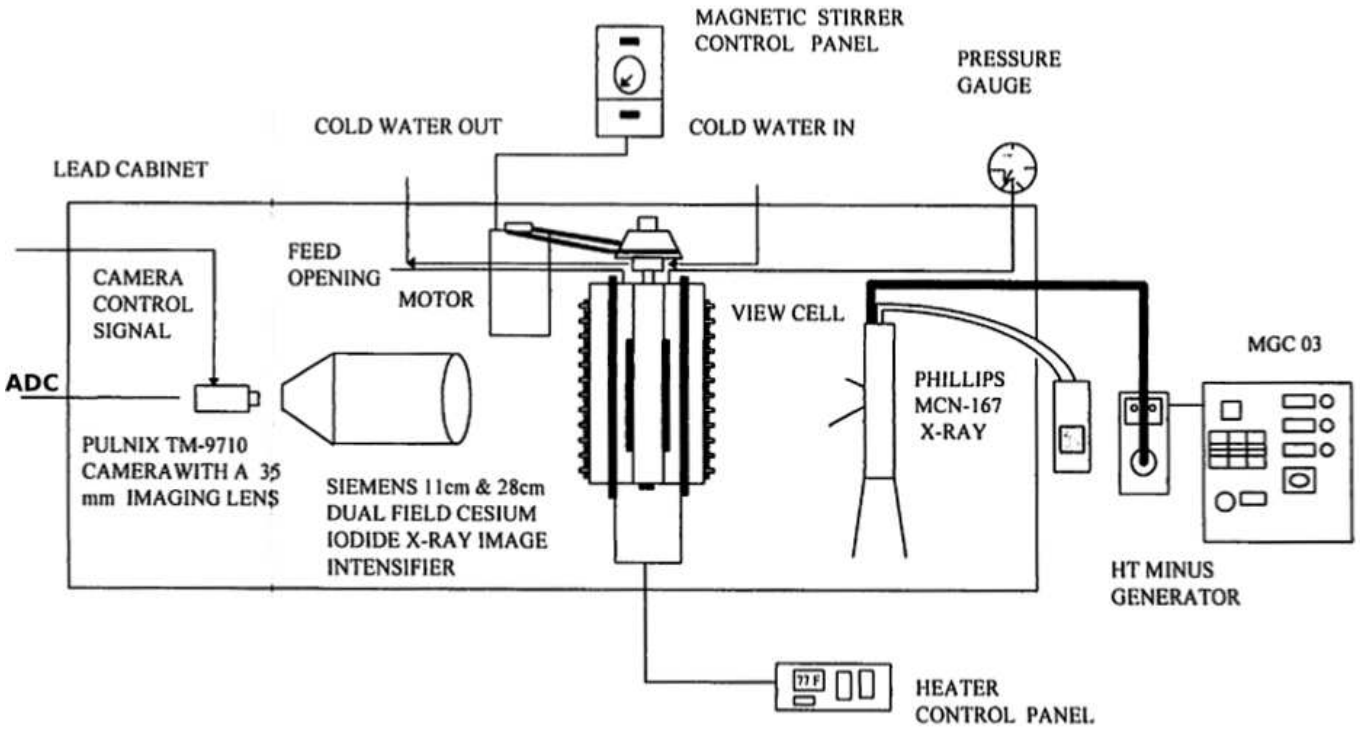

Fig. 1: The complete schematic of the X-ray view cell apparatus (Reproduced from Abedi (1998))

in intensity is not an important factor in our analysis as we use the physics only to estimate the approximate shape of the intensity profile in the images. The shape is largely unaffected by a scaling in the pixel intensities.

Fig 3 shows a typical X-ray image from this apparatus along with markings of the relevant regions. The base of the cell is at the left. The visual appearance of a phase is dependent upon its density and the mass absorbency (2). As the intensity of transmitted X-ray's decreases with an increase in the density, the corresponding image segment appears darker. Note that this is in contrast to traditional medical radiography.

For example, the vapor phase is the least dense and appears light. There are two liquid phases shown in this image and both of them have higher density than the vapor phase and hence look darker. The predominant dark area in the image corresponds to the non-hollow portion of the heating mantle which is used to maintain temperature of the cell. Note that the size and shape of the beryllium cylinder as seen in the image may vary. However, the orientation is always horizontal in the present study.

From these images, the volumes of all the phases can be obtained by computing the distance between the various interfaces and the base plate as the cross-sectional area of the hollow part of the Beryllium cell at any given elevation is known a priori. An automatic image processing algorithm is helpful in two ways :

1) Typically X-ray images are obtained very frequently and human marking of the interfaces is time consuming when a large volume of images are to be analyzed to investigate phase properties of fluids at different conditions.
2) Hand marking of the interfaces might not be accurate.

In this paper, we present an image processing method that can be used for automatic detection of all the interfaces present. As requirements for our algorithm we have the following:

1) Boundary detection must be precise. Sub-pixel accuracy is desired as small errors in the interface detection impact estimation of the phase equilibrium behavior.
2) The computational time of the algorithm should be very small to ensure large collections of images are processed quickly.

The paper is organized as follows. Section II describes the geometry of the set up, interface and region model. Section III discusses general edge detection and segmentation methods and gives results for two optimal edge detection algorithms. Section IV gives the novel region growing method used in interface detection. Section V provides the rule based procedure to find the interfaces and boundaries. In Section VI, results and comparison with the optimal filters and the proposed method are given. Section VII gives the concluding remarks.

II. Geometry and Region, Interface models

The image model given by Equation (2) provides information regarding the "shape" of the regions as observed in each scan line when the geometry is taken into consideration. Figure 4a gives the geometry of the set-up. The distance between the X-ray source and the detector is $a := d + e + f = 1.5m$ where $f = 0.5m$. The minimum path length $e = 0.12m$ occurs at about pixel number 300 (in the x direction) for the image

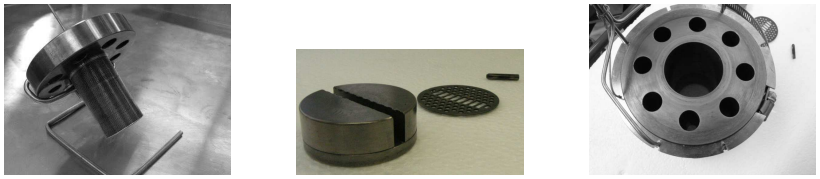

(a) Top plate with bellows (b) Beryllium insert, filter and the magnetic stirrer (c) Hollow Beryllium rod from top view

Fig. 2: Components of the X-ray view cell

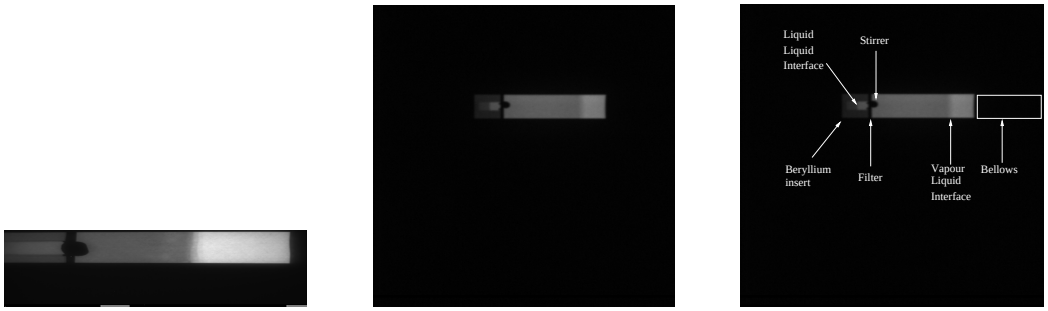

(a) Example X ray view cell image (b) Example X ray view cell image (c) Image with regions marked

Fig. 3: X-ray view cell image and markings

previously in Figure 3b. In other words, pixel number 300 is closest to the X-ray source in these images. For other pixels, the path length is longer. For a location on the detector at distance h from closest point to the source, the path length is $p(h) = e\sqrt{1+\frac{h^2}{a^2}}$ by simple geometry. Therefore, the intensity at this location is given by $I(h) = I_0 \exp(-\rho\mu p(h))$.

The image dimensions are 512×512 and hence approximately half of the cylinder is above the X-ray source and the other half below. Using the fact that $a = 1.5m$ and the total length of the Beryllium cylinder to be $0.15m$ the maximum variation in h is approximately $0.12m$ from the point on the detector corresponding to the minimum path length.

For many organic compounds used in the X-ray view cell $\mu \approx 0.23cm^2/g$ and $\rho \approx 0.85g/cm^3$. The variation in $\exp\left(-0.023\sqrt{1+\frac{h^2}{1.5^2}}\right)$ with h is depicted in Figure 4b.

Let the intensity change by the detector be described by

$$I_d(\lambda) = I(\lambda)\kappa$$

where κ is a characteristic of the detector therefore independent of the physical properties of the substance being analyzed for phase behavior. $I(\lambda)$ is the incident intensity of the X-rays on the detector.

Then, the observed intensity is given by

$$I_d(\lambda) = I_0(\lambda)\kappa \exp\{-\rho\Delta x\mu(\lambda)\}$$

Therefore, the observed intensity is only scaled by a factor. As values of I_0, κ change with experimental conditions we do not try to quantity deviation from linearity observed in Figure 4b. However, we note that, if we discount the factor $I_0\kappa$, the curve is approximately linear for small ranges of h. This is especially true for larger values of h as can be seen from Figure 4b.

Figure 5 shows a row (horizontal line) from the real image shown previously in Figure 3b. It can be observed that around pixel 300 the curve is more non-linear (note that this corresponds to $h \approx 0$) than for larger values of h. From this we can assume that the factor $I_0\kappa$ does not significantly alter the shape of the curve shown previously in Figure 4b. Note also the change in "slope" of the real data in Figure 5 about the pixel 300 as expected.

The vapour phase has $h \approx 0.02m$ and the variation in h is approximately $0.01m$ for this phase. For this small variation, the change in intensity should be approximately linear as mentioned before. This can indeed be verified in Figure 4b

As phases occupy only a small percentage of the overall image width, the assumption that variation is linear is valid. Importantly, these small variations from linearity do not seem to the affect the proposed method.

It can be further noticed from Figure 5 that the interfaces are approximately linear in nature. At interfaces, however, the variation is not just due to path length differences but also due to density and mass absorption co-efficient differences.

Based on the above observations, the region and interface models are assumed to be linear : the gray levels vary linearly at interfaces as well as within constant density regions (phases). Therefore, a region growing method configured to find linear patches can be used to find the interfaces and the phases simultaneously.

III. General Edge Detection and Segmentation Methods

In this section, a few methods for edge detection and segmentation relevant for the purpose of interface detection in X-ray view cells are reviewed. The interface and region models as obtained in the previous section are not enforced in these methods. We show results from the Canny method and one of its generalizations.

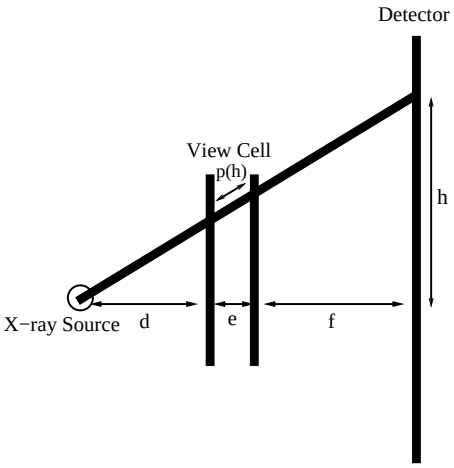

(a) Geometry of the Set-Up

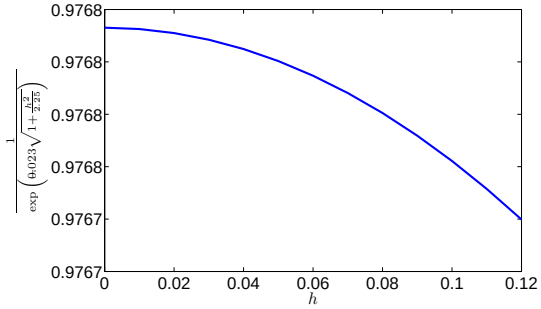

(b) Variation of pixel intensity for nominal values of $\rho = 0.85, \mu = 0.23, e = 0.15$

Fig. 4: Geometry producing approximate linear variation in pixel intensities for small ranges of h

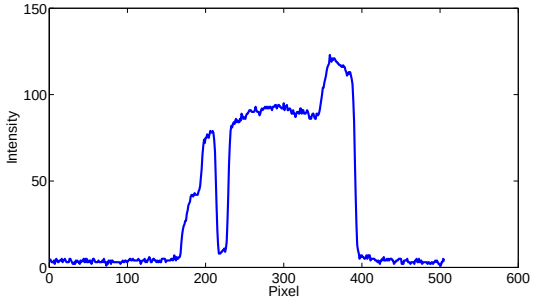

Fig. 5: A row inside the object of interest

A. *Edge Detection*

Canny edge detection uses first order derivatives but removes the weak edges by a process called non-maximum suppression, wherein responses which are not local maxima/minima are suppressed. After this, hysteresis thresholding is performed to trace the edges (Canny (1986)). In this method, the noise in the image is assumed to Gaussian. In X-ray images, the observed noise is Poisson. However, we present this method as it is considered to be a state of the art edge detection technique. The noise observed in the X-ray images in the current study is analyzed in Appendix A.

In the one dimensional setting of the current problem, it was found that hysteresis thresholding was not required as non-maximum suppression gives a gradient where there are no connected edges. Therefore, we use only one global threshold on the suppressed gradient. In practice it was observed that non-maximum suppression is very effective in removing spurious maxima/minima.

Figure 6a and 6b show the gradient and its non-maximum suppressed version for a row from the image shown in Figure 3a. Figure 6b shows the detected edges. Edge localization depends on the scale σ used in the Gaussian smoothing. To better illustrate this, variation of the detected location of the right interface with σ is shown in Figure 6c. It can be seen that for scales ranging from 6.0 to 10.0, the interface location varies by four pixels. For $\sigma < 6$ many spurious interfaces were detected so this case is not reported here.

For better edge localization, zero crossings of the second derivative can be used. Figure 7 shows the second derivative of the row focusing on the pixels near the right interface. The accurate location obtained by a visual reading for the location of the right interface is around pixel 483. It can be seen that the second derivative values are very small in the vicinity of the edge and no zero-crossing exists. This may be attributed to the noise present in the image. For accuracy, first and second derivative computation was performed using the filter taps given in (Farid & Simoncelli (2004)).

Canny's method is optimal for detecting step edges in images. Similar optimal filters for detecting edges resembling ramps (which are more relevant in the present study) are described in (Petrou & Kittler (1991)). As with the Canny method, it is assumed that image contains Gaussian noise. The edge model considered is

$$c(x) = \begin{cases} 1 - e^{-sx/2} & \text{if } x \geq 0 \\ e^{sx/2} & \text{if } x \leq 0 \end{cases}$$

where s controls the shape of the edge. The authors list the optimal filter coefficients for the convolution filter (edge

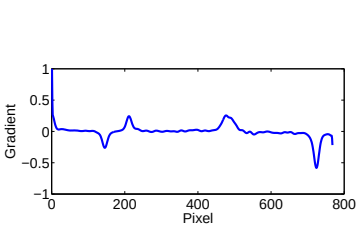

(a) Gradient with $\sigma = 6.0$

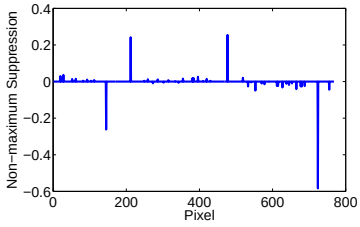

(b) Non-maximum suppressed gradient

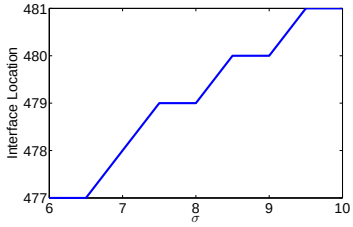

(c) Variation of the right interface with the smoothing standard deviation σ

Fig. 6: Canny Method

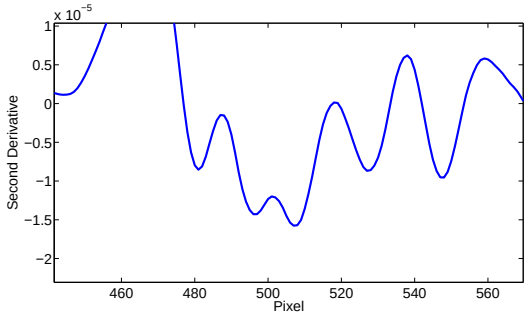

Fig. 7: Interface detection by Zero-crossings with $\sigma = 6.0$

detector). The filter used in the present analysis is

$$\begin{aligned} y(x) = &(exp(Ax)(K_1 sin(Ax) + K_2 cos(Ax)))+ \\ &+ (exp(-Az)(K_3 sin(Ax) + K_4 cos(Ax)))+ \\ &+ K_5 + (K_6 exp(sx)) \ \forall x \leq 0 \end{aligned} \tag{3}$$

$$\begin{aligned} A &= 1.42 \\ K_1 &= 0.028 \\ K_2 &= 1.737 \\ K_3 &= -0.113 \\ K_4 &= -0.055 \\ K_5 &= -1.33 \\ K_6 &= -0.35 \end{aligned}$$

For $x > 0$, $y(x) = -y(-x)$ is used. Figure 8a shows the convolution of the row with such a filter. This method was observed to be robust for limited variation in s and w (where w is the filter width). However, the base of the view cell and the edge below the liquid-liquid interface also have significant gradient values when compared to the actual interface. From Figure 8b it can be seen that (near pixel 200) a threshold needs to be fine tuned to extract the liquid-liquid interface on the left side.

A heuristic method for detecting the left interface can still be obtained in spite of the above mentioned issue. For example, as there is only a single interface present in the Beryllium insert, the edge with the largest possible x-value can be considered to be an interface. However, an important problem with methods based on convolution is that detection of interfaces near the image boundary is an error-prone process. This problem arises due to lack of sufficient data for gradient estimation. The problem is amplified if the filter width is large. More results on the two methods are showed in Section VI where the problem of detection of interfaces near the boundary is also discussed.

In the paper (Elder & Zucker (1998)) the variance of the noise is taken into account for computing derivatives. The authors derive conditions for the existence of a nonzero gradient at a point in the image by computing the probability that the gradient is not the response of noise alone. This criteria is expressed in terms of the second moment of the sensor noise and the scale of the derivative of Gaussian operator used to detect the edges. Similar formulae are also derived for the second derivative operators.

A unique minimum reliable scale is computed at every pixel location by using the above criterion. From this, derivative estimates at these scales are obtained and zero crossings detected. These locations give the edges. Note that this method is easily applicable only when the sensor noise is constant throughout the image and not a function pixel location or intensity.

In the current set of images, the noise observed in the image is not constant and varies with the location of the pixel. Therefore, the method does not directly apply to the present situation.

B. Segmentation

The interfaces can also be detected as the boundaries of the regions resulting from a segmentation algorithm. The Mumford-Shah model is one of the standard models for image segmentation in the energy minimization framework. The piece-wise constant restriction has been thoroughly analyzed in the original paper (Mumford & Shah (1989)).

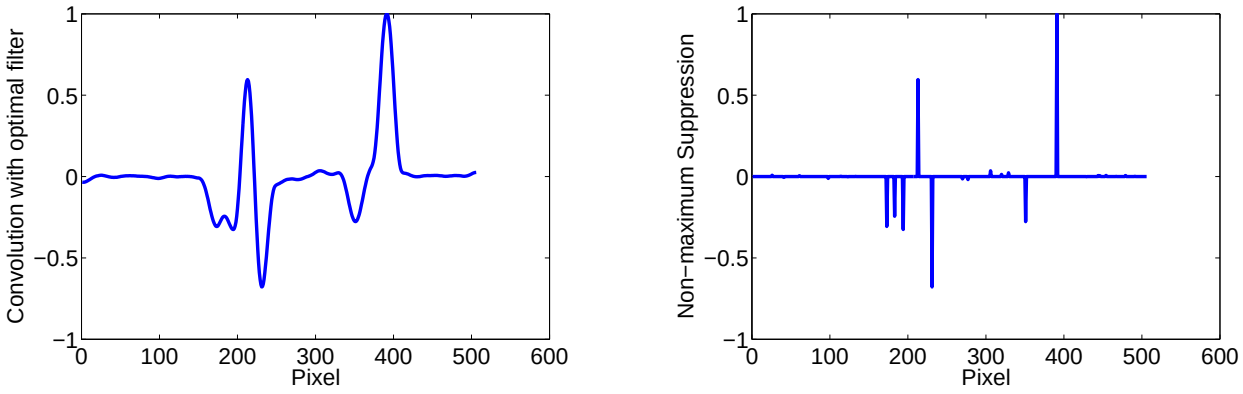

(a) Result of optimal edge detector for ramp edges

(b) Non-maximum suppression of the result

Fig. 8: Detection of Ramp Edges, with $s = 1, w = 2$ (w is filter width)

Much attention has been given to curve evolution methods for finding local minima of the energy functional for images containing *two regions* (Chan & Vese (2001)), which rely on gradient descent for optimization. Typically, curve evolution methods depend on the initialization of the contour and are relatively slower when compared to the combinatorial approaches discussed next.

Recently, combinatorial optimization techniques have been used (El-Zehiry et al. (2011); Leo & Chirstopher (2009)) for obtaining solutions to the piece-wise constant and the piece-wise smooth versions. Both of these approaches try to obtain the global minimum instead of the local minima typically attained in curve evolution methods.

Both the papers cited above describe binary image segmentation (i.e. segmenting the image into foreground and background regions). In the second paper, the combinatorial analogue of the Mumford-Shah model is developed first. The optimization is then split into two parts: solving for f, g (where f is the foreground and g is the background) given the boundary and then solving for the boundary given f, g. This process is repeated until convergence. The optimal f, g given the boundary are obtained in a straight-forward manner. For computing, the optimal boundary given f, g, the method requires the estimation of f, g outside the foreground and background regions respectively.

The literature available for multi-region segmentation in two-dimensions using curve evolution or combinatorial methods is small compared to the two region case. 2D global segmentation techniques such as these might not provide sub-pixel accuracy as desired in the present method. Omission of the correct region and interface (edge) models into these general edge detection or segmentation methods might affect their performance. However, these methods are useful when no such models are available apriori.

In the next section, we present an image segmentation method based on the Mumford-Shah model configured to detect linear patches. The advantage of this method over the gradient based methods is two fold:

1) Robustness of detection over a large range of input parameters
2) Sub-pixel accuracy for interface detection
3) Interfaces near the boundary of the image can also be accurately retrieved

IV. Region growing method for interface detection

A. Mumford Shah model

One of the canonical approaches for image segmentation is the minimization of the Mumford Shah energy functional (Mumford & Shah (1989)). The minima of the functional is the desired segmentation. The Mumford Shah functional is defined as :

$$E(f, K) = \int_{\Omega} (f - g)^2 d\mu + \int_{\Omega \setminus K} |\nabla f| d\mu + \lambda \sigma(K) \quad (4)$$

where the first term prohibits the solution f from being very different from g, the second term ensures that in each region f is smooth and the last term measures the total length of the boundary between the regions. Here μ and σ are the two dimensional Lebesgue and Hausdorff measures respectively.

In the case when f is assumed to be piece-wise constant, it is known that there exists a minimizer to (4) (Mumford & Shah (1989); Morel & Solimini (1995)). Local minima can be found using a region merging algorithm as described by (Koepfler et al. (1994)). Note that in this case, the second term vanishes and the f which minimizes the first term is the mean of g in each of the regions.

The piece-wise constant assumption is not appropriate here as the regions do not have a constant gray level. As noted before the gray levels vary linearly inside each region. We therefore modify the Mumford Shah energy to incorporate a linear interface and region model. A one dimensional modification of the Mumford Shah model is described next.

B. Modified Mumford Shah Model

The new energy functional is defined as:-

$$E(f, K) = \int_{\Omega} (f - g)^2 dx + \lambda |K| \quad (5)$$

where f is constrained to be a combination of linear regions (i.e. f is piece-wise linear), $|K|$ is the cardinality of the set of all end-points of the linear regions. As before, λ gives the penalty for maintaining more regions and g is the source line. Note that this model is a generalization of the piece-wise constant model. Therefore, regions of constant pixel intensities can also be detected by this method.

A region merging algorithm can be used to obtain a local minima for (5). More specifically, all points on the scan line are initially assumed to be individual regions. Each region is represented by two points: $(i, a_i), (j, a_j)$, the first point is the initial point of the straight line describing the region and second point is the end point of this line. In the beginning, both these points coincide for all the regions. Here i represents a location in the row whereas a_i represents the reconstructed intensity at that location.

Adjacent regions are selected for merging if the merged region (represented by a straight line connecting the end points of the two regions) has smaller energy than the combined energy of the two regions. More precisely, if $(i_1, a_{i_1}), (i_2, a_{i_2})$ and $(j_1, a_{j_1}), (j_2, a_{j_2})$ are the two regions, the merged region is represented by $(i_1, a_{i_1}), (j_2, a_{j_2})$ assuming without loss of generality that $i_1 < j_2$. If the original segmentation is f_1 and f_2 is the segmentation after merging, the energy difference is $\Delta E = \int_\Omega (f_2 - g)^2 dx - \int_\Omega (f_1 - g)^2 dx - \lambda$. If $\Delta E < 0$ then the regions are merged. The process is repeated until no merging is possible.

If a region R is described by $y = mx + C$ where $x \in [a, b]$, the error of the segmentation $\int_{\Omega \cap R} (f - g)^2$ in this region is computed by projecting each of the pixels of the row in the range $[a, b]$ on to the straight line and summing up all these errors. For obtaining the total error $\int_\Omega (f - g)^2$, all the errors for individual regions are added.

At any given stage there might be many adjacent regions whose merging decreases the overall energy. In this case, the regions whose merging gives the smallest energy decrease are merged. We summarize the steps below (let g be the original row).

1) Initialization: Each pixel in the scan line is represented by $(i, a_i), (i, a_i)$ where i is the location of the pixel and a_i is the pixel intensity at that location. Tag each region with an error term equal to zero. (Denote by $e(i)$ the error of region i).
2) For every pair of adjacent regions $R_1 = \{(i_1, a_{i_1}), (i_2, a_{i_2})\}$ and $R_2 = \{(j_1, a_{j_1}), (j_2, a_{j_2})\}$ (with $i_1 < j_1$)
   a) Project $g(k)$ $\forall k, i_1 \leq k \leq j_2$ onto the straight line determined by the two end points, (i_1, a_{i_1}) and (j_2, a_{j_2}). Let the projections be given by $g_p(k)$. Compute $\sum_k g_p(k)$.
   b) $\Delta E = \sum_k g_p(k) - e(R_1) - e(R_2) - \lambda$. If $\Delta E < 0$, then select these regions as potential candidates for merging.
3) Find the regions whose merging gives the maximum energy reduction.
4) Go to step two and repeat until no two regions exist for which $\Delta E < 0$.

Note that no assumptions on the noise are made in the region growing method. In fact, based on a noise model of the pixels in a single region, the region growing method can be enhanced. However, as shown in Appendix A, the Poisson noise model with constant mean inside the phases, is not a true reflection of the actual noise observed in the image. The fact that mean is not constant within a phase also follows from the earlier analysis as the intensity was seen to vary linearly.

V. Edge Localization using a Stage-Wise Procedure

The result of the segmentation depends on the value of λ. In a typical image, all the phases are not separated by a large difference in pixel intensities. When an interface separates two phases whose mean intensity difference is low, a smaller value of λ is required. Larger values of λ will merge the two phases as a single region.

Hence, the final interfaces are detected in a stage-wise fashion by using multiple λ's. Note that, when $\lambda = 0$, no merging is done and for $\lambda = \infty$, all pixels will fall under a single region. We now describe a rule based procedure to identify the phase boundaries.

A. Procedure

The base of the cell, the edge below the liquid-liquid interface and stirrer location do not vary for experiments in a given set-up. Therefore, this information is given apriori to the algorithm. Similarly the object has the same y co-ordinates throughout a set of experiments. Therefore, detection of boundaries in the y-direction is not performed. Using the given y-co-ordinates the center row is chosen for analysis.

Note that y-co-ordinates can be found using the present analysis in the y-direction. However as the aim is to obtain precise location of the boundaries, information that is known to be constant in a given set of experiments is directly used as input to the algorithm to reduce the errors in boundary localization.

By separating the row as left and right parts to the stirrer, different values of λ can be used for the left and the right parts of the row (say λ_l, λ_r). This is required as the interfaces on the left side have been observed to be very faint as compared to the interfaces in the right part. For example, Figure 9 shows segmentations using two different values of λ on the right and left parts. Note that the given row is divided into the left and right parts based on the specified location of the stirrer.

To avoid fine tuning the values of λ_l, λ_r for different set-ups, we assume that the number of interfaces in the left and right parts of the image are known. For a range of temperatures and pressures, the number of interfaces on either side does not change. Therefore, the assumption that number of interfaces are known is not too restrictive. If l interfaces are present in the left part, l regions are chosen based on regions with maximum slope. Similarly, if r interfaces are present in the right part, r regions are chosen depending on maximum slope.

The extreme right boundary of the object varies from image to image so it is not known apriori. This boundary is estimated

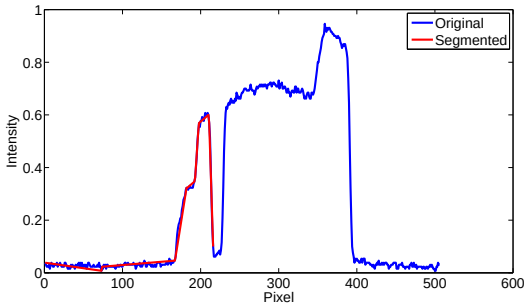

(a) Fine segmentation with $\lambda_l = 0.01$ for detection of interfaces in the left part

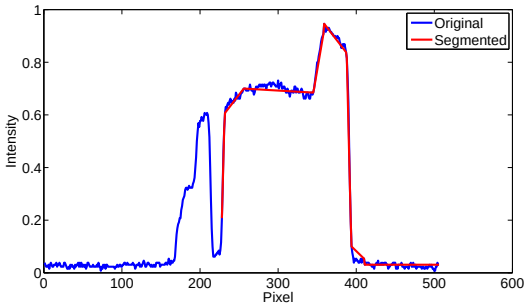

(b) Coarser segmentation on the right part with $\lambda_r = 0.1$

Fig. 9: Segmentation with different values of λ

by considering the line segment with the largest negative slope in the right part of the row.

All the interfaces and boundaries are marked as the mid-points of the corresponding line segments. This gives sub-pixel accuracy for interface detection. The result using the method just described is shown in Figure 10.

VI. Results and Comparison

In this section, we compare the results from the proposed method with interface readings obtained manually on a set of forty images similar to the image shown in Figure 3a. These images are obtained to study the phase behaviour of Bitumen + Water.

In Figure 11a the results for detection of the interface on the right part are shown. The original values are eye readings, where the interface location is taken to be the mid-point of the ramp part of the edge. The results for the Canny method shown here are after removing spurious detections on three images. In one instance, this was due to boundary effects (i.e. lack of data across the boundary of the image to apply smoothing and derivative operators) and in the other two the spurious detections were because of a high threshold ($t = 0.2$ on the normalized non-maximum suppressed gradient was used). Reducing the threshold to $t = 0.1$ resulted in many spurious edges.

Interestingly, in all the these three images the proposed method gave accurate results. This can be attributed to the fact that the proposed method does not rely on convolution operations and therefore does not require image data beyond the boundary. Also, as gradient computation is not performed, the method is more robust to small local changes in pixel intensity.

Further, for the image shown in Figure 3a, the interface location was constant at 483.5 for all $0.03 \leq \lambda_r \leq 0.1$ in the proposed method. This is in contrast to the Canny method where the detected interface location changes with σ. This shows that the proposed method is very robust to a large range of input parameters.

Figure 11b shows similar results for the detection of the extreme right boundary of the view cell. In this case, the spurious detection by the Canny method has been shown. This error resulted as non-maximum suppression failed to detect the right boundary as a maximum point due to lack of data towards the right of this boundary.

Errors	Right Interface	Right Boundary
Proposed	136 (C), 160 (P)	330.5 (C), 330.5 (P)
Canny	177.5	351
Petrou	169.5	325

TABLE I: Comparison of errors of the proposed method with Canny (C) and Petrou (P) methods. Note that two different values for C and P are given corresponding to the proposed method as the spurious detections were different in both the cases. The errors mentioned were after removing these.

Finally, Figure 12 shows the comparison for the method in Petrou & Kittler (1991) (we shall refer to this method as Petrou below). One spurious detection was observed on the same image for which the Canny method failed. Again, this is due to lack of data for gradient estimation near boundary.

To check the accuracy, sum of absolute differences of the original and the proposed method are computed. Similar values for the Canny method and the Petrou method are computed. All of these values are tabulated in Table 1 after removing the spurious detections from the Canny and the Petrou methods.

In the Table, C and P refer to Canny and the Petrou methods, respectively. We list two different values as the spurious detections were different in both cases.

It can observed from Table I that the current method outperforms the Canny method in terms of accurate detection of interface locations. The proposed method gives better accuracy compared to the Petrou method for interface detection whereas the Petrou method is slightly better for Boundary detection. Note that this is after removing the spurious detections.

Overall, the proposed method gives robust estimates near image boundaries and is very accurate. Also, the method is stable for a large range of input parameters as observed previously.

VII. Conclusions

In this paper, we analyzed the image generation process to obtain a region and edge model of the X-ray images. Based on this a novel extension of the region merging algorithm has

(a) An example detection with $\lambda = 0.1, \lambda_l = 0.01, \lambda_r = 0.1, l = 1, r = 1$

(b) An example detection with $\lambda = 0.1, \lambda_l = 0.01, \lambda_r = 0.1, l = 0, r = 1$

Fig. 10: Detection along the x-direction

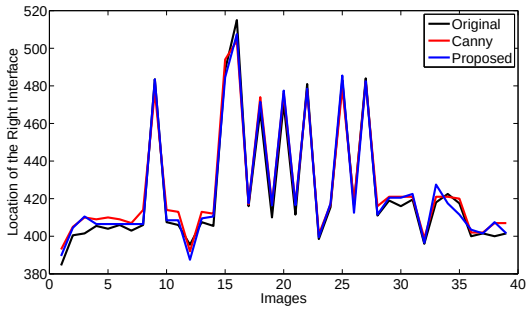

(a) Detection of the phase boundaries in the right part. Error for the current method is 136 whereas for the Canny method the error is 177.5. Canny method is used with $\sigma = 6.0$ and threshold of $t = 0.2$ on the normalized non-maximum suppressed gradient

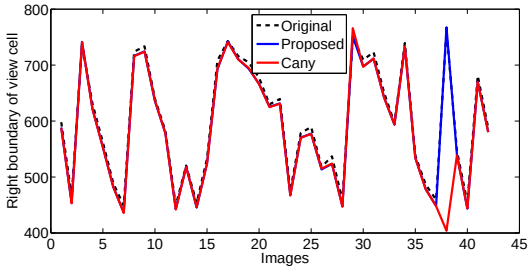

(b) Detection of the extreme right boundary of the view cell using $t = 0.2$ and $\sigma = 6.0$ as before

Fig. 11: Comparison of original and detected interface and boundary

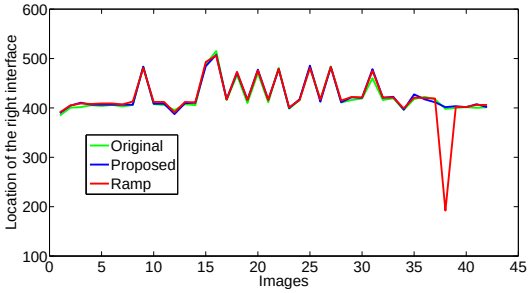

(a) Detection of the interface in the right part using the convolution filter given in Eq 3 and threshold of $t = 0.2$ on the normalized non-maximum suppressed gradient

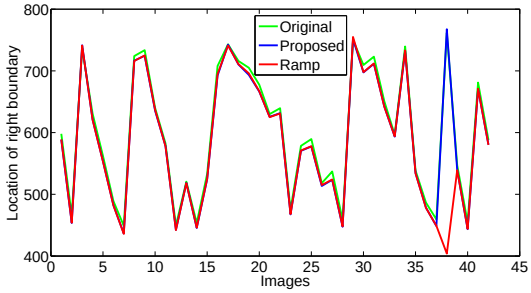

(b) Detection of the extreme right boundary using the same method

Fig. 12: Comparison of original and detected interface and boundary using the method in Petrou & Kittler (1991)

been proposed. The new method consists of approximating each region and edge as a straight line segment. Using simple rules derived from the structure of the image, the approach automatically discovers the regions and the precise location of the interfaces. It was observed that the proposed method is robust to changes in the input parameters and detection of edges near image boundary. The interfaces and boundaries were detected to sub-pixel accuracy. The proposed method is compared with general methods and it was observed that results obtained with respect to accuracy of edge detection are superior.

Appendix A
Noise Model

It is known that the noise observed in X-ray images is Poisson distributed.

$$P(X = k) = \frac{\lambda^k e^{-\lambda}}{k!}$$

where, X is the observed intensity in a given phase and λ is the mean value of pixel intensities in the phase.

Hypothesis testing is carried out to know if the pixels in a given region are generated from the same Poisson distribution. We consider the statistic described in (Brown & Zhao (2002)). The method is based on the variance stabilizing transformation of Anscombe. The null hypothesis and the test statistic

considered are :

$$\begin{aligned} H_0 &: X_i \sim Poiss(\lambda) \\ T &= 4\sum_{i=1}^{n}(Y_i - \bar{Y})^2 \end{aligned}$$

where, $Y_i = \sqrt{X_i + \frac{3}{8}}$ and $T \sim \chi^2_{n-1}$. The test statistic has approximately χ^2_{n-1} distribution. From this, H_0 is rejected at confidence level $1-\alpha$ if $T > \chi^2_{n-1,1-\alpha}$.

The number of pixels in all the regions is observed to be at-least two hundred. For large n, T is close to a Gaussian distribution with mean and variance $(n-1)$, $4(n-1)$ respectively (here n is the number of pixels in the region). The p-values for most of the regions were insignificant (very close to zero) and therefore the null hypothesis that all the pixels in a given phase are independent realizations of the same Poisson distribution is rejected. This is due to the change in pixel intensity within a phase due to the variation of the path length of the X-rays as was observed in Figure 5.

REFERENCES

Jalal Abedi (1998). *Unusual Retrograde condensation and Asphaltene Precipitation in Model Heaw Ol Svstems Using X-ray Imaging*. Ph.D. thesis, University of Toronto.

S. J. Abedi, H.-Y. Cai, S. Seyfaie, & J.M. Shaw (1999). 'Simulatneous phase behaviour, elemental composition and density measurement using x-ray imaging'. *Fluid Phase Equiibria* .

Lawrence D. Brown & Linda H. Zhao (2002). 'A test fot the poisson distribution,'. *Sankhya: The Indian Journal Of Statistics* .

J. Canny (1986). 'A computational approach to edge detection'. *IEEE Transactions on Pattern Analysis and Machine Intelligence* **8(6)**.

Tony Chan & Luminita Vese (2001). 'Active contours without edges'. *IEEE transactions of Image processing* **10**.

Noha El-Zehiry, Prasanna Sahoo, & Adel Elmarghraby (2011). 'Combinatorial optimization of the piecewise constant mumford-shah functional with application to scalar/vector valued and volumetric image segmentation'. *Image and Vision Computing,* **29**(11):365–381.

J.H. Elder & S.W. Zucker (1998). 'Local scale control for edge detection and blur estimation'. *IEEE Transactions on Pattern Analysis and Machine Intelligence* **20(7)**:699 – 716.

Hany Farid & Eero Simoncelli (2004). 'Differentiation of discrete multi dimensional signals'. *IEEE Trans. Image Processing* **13**(4):496–508.

C. Koepfler, C. Lopez, & J.M. Morel (1994). 'A multiscale algorithm for image segmentation by variational method'. *SIAM JOURNAL OF NUMERICAL ANALYSIS* pp. 282–299.

Grady Leo & Alvino Chirstopher (2009). 'The piecewise smooth mumfordshah functional on an arbitrary graph,'. *IEEE Transactions on Image Processing,* **18**(11):2547–2561.

Amani Mohammad, M.R. Gray, & J.M Shaw (2013). 'Volume of mixing and solubility of water in athabasca bitumen at high temperature and pressure,'. *Fluid Phase Equiibria* .

Jean-Michel Morel & Sergio Solimini (1995). *Variational Methods in Image Segmentation*. Birkhauser.

David Mumford & Jayant Shah (1989). 'Optimal approximations by piecewise smooth functions and associated variational problems,'. *Communications on Pure and Applied Mathematics,* **XLII**(5):577–685.

Maria Petrou & Josef Kittler (1991). 'Optimal edge detectors for ramp edges'. *IEEE Transactions on Pattern Analysis and Machine Intelligence* pp. 483–491.

X. Zhang & J. M. Shaw (2006). 'Impact of multiphase behavior on coke deposition in heavy oils hydroprocessing catalysts'. *Energy & Fuels* **20**:473 – 480.

X.Y. Zou & J.M. Shaw (2006). *Phase Behaviour of Heavy Oils*, chap. Asphaltenes, Heavy oils and petroleomics, pp. 485 – 505. Mullins ed.

Phanindra Jampana obtained his B.Tech in Chemical Engineering from IIT Madras, India in 2004 and the Ph.D. degree in Process Control from the University of Alberta, Edmonton, Canada in 2010. He joined the Department of Chemical Engineering at IIT Hyderabad in 2011 where he is currently an Assistant Professor.

Sirish L. Shah has been with the University of Alberta since 1978, where he is currently Professor of Chemical and Materials Engineering. While at the University of Alberta he held the NSERC-Matrikon-Suncor-iCORE Senior Industrial Research Chair in Computer Process Control from 1999 to 2012. He has held visiting appointments at Oxford University and Balliol College as a SERC fellow , Kumamoto University (Japan) as a senior research fellow of the Japan Society for the Promotion of Science (JSPS) , the University of Newcastle, Australia, IIT-Madras, India and the National University of Singapore. The main area of his current research is process data analytics involving process and performance monitoring, design of smart alarm systems, system identification and design and implementation of softsensors.

John Shaw obtained his B.A.Sc. degree in Chemical Engineering and his Ph.D. in Metallurgy and Material Science at the University of British Columbia, Vancouver, Canada in 1981 and 1985 respectively. In 1985, he joined the Department of Chemical Engineering and Applied Chemistry at the University of Toronto, where he rose to the rank of professor. In 2001, he joined the Department of Chemical and Materials Engineering at the University of Alberta where he holds the NSERC industrial research chair in petroleum thermodynamics. In his current role he develops enabling technologies, and methodologies for measuring and calculating thermophysical properties of hydrocarbons, and for selecting industrial processes related to the hydrocarbon production, transport and refining sectors. He is the theme leader for Carbon Management Canada (a Canadian national centre of excellence) and he is an associate editor of Energy and Fuels. He has an interest in engineering design and e-learning, and he likes to ride bicycles and travel!